
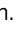


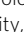



Large-scale photovoltaic solar farms in the Sahara affect solar power generation potential globally

Jingchao Long^{1,2,3,4,11}, Zhengyao Lu^{2,11}, Paul A. Miller², Julia Pongratz⁵, Dabo Guan⁶, Benjamin Smith^{2,7}, Zhiwei Zhu⁸, Jianjun Xu^{1,3,9} & Qiong Zhang¹⁰

Globally, solar projects are being rapidly built or planned, particularly in high solar potential regions with high energy demand. However, their energy generation potential is highly related to the weather condition. Here we use state-of-the-art Earth system model simulations to investigate how large photovoltaic solar farms in the Sahara Desert could impact the global cloud cover and solar generation potential through disturbed atmospheric teleconnections. The results indicate negative impacts on solar potential in North Africa (locally), Middle East, Southern Europe, India, Eastern China, Japan, Eastern Australia, and Southwestern US, and positive impacts in Central and South America, the Caribbean, Central & Eastern US, Scandinavia and South Africa, reaching a magnitude of $\pm 5\%$ in remote regions seasonally. Diagnostics suggest that large-scale atmospheric circulation changes are responsible for the global impacts. International cooperation is essential to mitigate the potential risks of future large-scale solar projects in drylands, which could impact energy production.

¹ College of Ocean and Meteorology/South China Sea institute of marine meteorology (SIMM), Guangdong Ocean University, Zhanjiang, China. ² Department of Physical Geography and Ecosystem Science, Lund University, Lund, Sweden. ³ Shenzhen Institute, Guangdong Ocean University, Shenzhen, China. ⁴ Key Laboratory of Climate, Resources and Environment in Continental Shelf Sea and Deep Sea of Department of Education of Guangdong Province, Guangdong Ocean University, Zhanjiang, China. ⁵ Department of Geography, Ludwig Maximilian University of Munich, Munich, Germany. ⁶ Department of Earth System Science, Tsinghua University, Beijing, China. ⁷ Hawkesbury Institute for the Environment, Western Sydney University, Penrith, NSW, Australia. ⁸ School of Atmospheric Sciences, Nanjing University of Information Science and Technology, Nanjing, China. ⁹ CMA-GDOU joint laboratory for Marine meteorology, Guangdong Ocean University, Zhanjiang, China. ¹⁰ Department of Physical Geography and Bolin Centre for Climate Research, Stockholm University, Stockholm, Sweden. ¹¹ These authors contributed equally: Jingchao Long, Zhengyao Lu. ✉email: longjc@gdou.edu.cn; zhengyao.lu@nateko.lu.se

Globally, renewable carbon-free energy is gradually replacing fossil fuels¹. Solar energy can be a major player in the increasing supply of renewable energy that reduces carbon emissions as an essential component of climate mitigation strategies². A recent study³ suggests that the share of solar energy in the world's total energy consumption has the potential to rise to as high as 76% by 2050 in a feasible energy transition scenario, from 1% in 2015 due to the cost effectiveness and the excellent resource distribution across the world⁴.

Solar power generation relies on solar irradiance—the amount of available sunlight at a particular location. Its potential can be quantified using the climate variable surface downward shortwave radiation (RSDS), defined within the wavelength interval 0.2–4.0 μm . Apart from its daily and seasonal cycles, weather-induced cloud variability affects RSDS. Under a fully cloud-covered sky (no rain), the solar radiation reaching the surface is reduced by about 75%⁵. The unpredictable variations in RSDS, mainly caused by weather conditions, pose difficulties for the stability of electricity supply of a solar power system⁶. In practice, the changes of solar system energy output are taken into account by grid operators in order to schedule the spinning reserve capacity and to manage the grid operations⁷.

As the solar industry grows, solar power generation is becoming increasingly weather-dependent⁸. Some studies have focused on the impacts of climate change on solar power generation in various future climate scenarios (for a review, see ref. ⁹). A general trend in climate change projections seems to be decreased cloud cover in low- to mid-latitude regions¹⁰. The changes in irradiation for different regions, seasons, timeframes and scenarios seldom exceed $\pm 10\%$ ⁹.

However, the global climate pattern can also be disturbed by massive deployment of solar energy. This is attributed to the resultant changes in land surface properties (e.g., the surface albedo, roughness)^{11,12}. In particular, recent modeling studies show that the regional climate response to solar panels in arid regions (e.g. North Africa) can be amplified through local atmosphere-land and vegetation feedback processes^{13,14}. This may further lead to disturbance in the global climate and hence the global solar power production.

We aim to quantify the impacts of a large-scale deployment of photovoltaic solar farms in the Sahara on global solar power generation as a pilot case study, and investigate the underlying forcing mechanisms. We use a state-of-the-art, fully-coupled Earth system model (EC-Earth) and consider three solar energy production scenarios in North Africa covering 5%, 20% and 50% of that region (hereafter S05, S20, S50; Methods; Supplementary Fig. 1). In previous studies^{13,14} the global climate and vegetation cover responses to these hypothetical Sahara solar farms were investigated, and here we focus more explicitly on how the global solar power generation itself can be affected.

Results

Changes in global cloud fraction and RSDS. The Earth system model simulations show that the annual mean global cloud fraction response is proportional in S05, S20 and S50, with limited significant response in S05, and more evidently redistributed cloud cover by the large-scale Saharan solar farms in S20 and S50 (Fig. 1a–d). The largest response in cloud fraction is locally over North Africa, with a center of anomalous cloud in the Sahel region. The positive cloud fraction anomaly only covers a small region and barely exceeds 1% in S05, but is much expanded and intensified in S20, reaching over 5% and covering half of North Africa. This anomaly extends northward to Southern Europe and eastward to the Southern Arabian Peninsula in S20. Other major land regions experiencing increased annual mean cloud fraction

include India, North Asia, and Eastern Australia. Conversely, decreased cloud cover is observed over Central and South America, South Africa, Central & Eastern United States, Central Asia and Northwestern China.

Seasonally, the response in the global cloud fraction, and in turn, RSDS, is generally stronger during the Northern Hemisphere (NH) summer season than its winter season (Fig. 2). This can be attributed to enhanced local atmosphere-vegetation feedbacks in North Africa associated with an intensified Western African Monsoon (Supplementary Fig. 2a, b)¹⁴. In the Southern Hemisphere, the South American and South African regions both show stronger austral winter (NH summer, June–July–August, JJA) cloud changes, linking these changes to remote impacts from North Africa. The exception is Eastern Australia, where cloudier conditions are larger during December–January–February (DJF), implying an indirect response due to Walker circulation changes (explained below).

RSDS changes largely follow the cloud fraction changes (Fig. 1e–h), with increased (decreased) RSDS mainly attributed to decreased (increased) cloud fraction. Some minor disagreement between cloud fraction and RSDS changes can be explained by other cloud-related properties such as albedo and lifetime¹⁵, and will not be discussed in this study. Seasonal RSDS anomalies reveal a robust response which turns out to be smoothed out in annual mean changes, particularly noticeable in S20 and S50. For instance, decreased RSDS in Northeast Asia during JJA, increased RSDS surrounding the Caribbean and Scandinavia during JJA, and increased DJF RSDS in South Africa are much weakened in annual mean differences. On interannual timescales, RSDS variability (interannual standard deviation) decreases most prominently in the tropical Pacific (Supplementary Fig. 3) due to suppressed ENSO variability¹⁴. However, the opposite response of interannual RSDS variability in S20 and S50 in many regions (e.g., Northern US in ANN, Eastern Australia in DJF, India in JJA) suggest that it is likely to be governed by regional-scale processes¹⁶.

Impacts on solar power generation. We next examine how the global PV power generation is affected by large-scale solar farms in the Sahara in our simulations. Figure 3 summarizes the changes in PV power generation potential (PVpot; Method) averaged over the whole year, JJA and DJF. Predominantly, the PVpot changes (Fig. 3) are attributed to RSDS changes, as an in-phase change of RSDS and PVpot are found in most regions. The magnitude of PVpot change is mostly negligible in S05, except for a less than 3% seasonal decrease in western Sahel and a less than 5% increase in South Africa (Fig. 3b1–b3). The annual PVpot increase in Southeast Asia is not in agreement with the other two scenarios, and likely arise from model internal variability. In S20 and S50, more robust PVpot changes are captured by the model (Fig. 3c1–c3, d1–d3). In North Africa, the Middle East, Europe excluding Scandinavia, India, Eastern China, Japan, Eastern Australia, and Southwestern US, PVpot during the local summer season is reduced. This change is in most cases large enough to result in an annual drop in PVpot. PVpot in some other regions benefits from the remote forcing, for instance, in Central and South America, the Caribbean and Central & Eastern US, Scandinavia, and South Africa. About -4% annual change for S20 is simulated for regions more sensitive and/or closer to the source of disturbance, e.g., in North Africa, Central Europe and India. During the high solar energy production season (i.e., local summer) these changes in PVpot of S20 are considerably larger, exceeding -8% for a sizeable region of North Africa, and over $\pm 5\%$ in India and Northern US, parts of Central and South America and $\pm 3\%$ for Europe, Southwestern US and South Africa

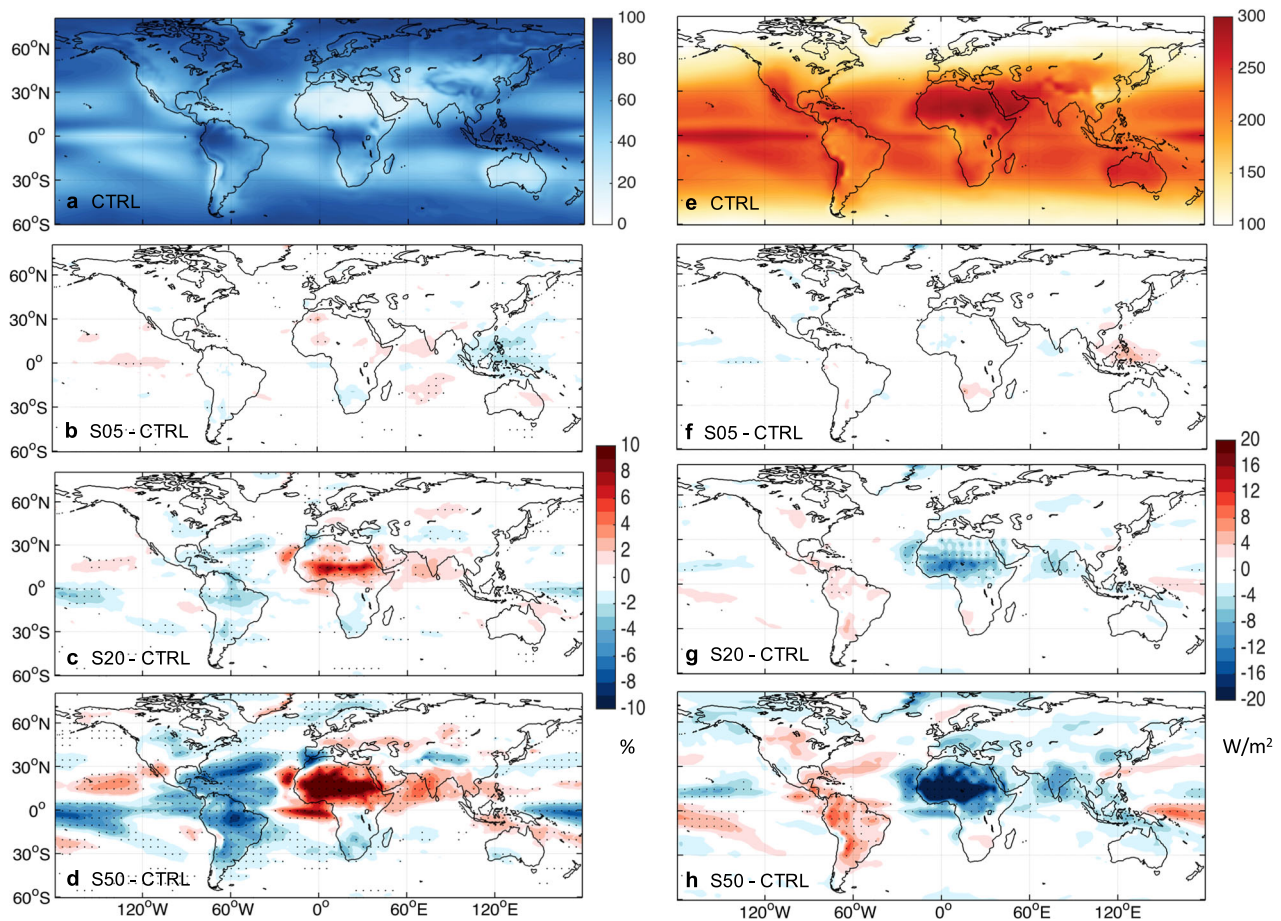


Fig. 1 Global cloud cover and shortwave radiation affected by Sahara solar farms. Modeled annual mean (ANN) (a) total cloud fraction and (e) RSDS in CTRL, and (b-d) total cloud fraction and (f-h) RSDS response in S05, S20 and S50. Black dots in b-h depict anomalies that exceed 95% significance in a *t* test.

and (Fig. 3c1–c3). The significance level of the responses in PVpot is highly dependent on its interannual variations (Supplementary Fig. 4). The magnitude of robust changes in PVpot for these regions are comparable to previous studies which investigated similar impacts of climate change on solar energy production in a fossil-fuel-dependent pathway (e.g. $\pm 10\%$ in SSP5-8.5^{17–19}). It should be pointed out that when averaged over large regions such as continents (Supplementary Table 1) and countries (Supplementary Table 2), the PVpot changes are quite muted and limited to $\pm 2\%$.

Climate forcing mechanisms. Our model results, specifically S20 and S50, demonstrate that the atmospheric circulation changes induced by the Sahara PV solar farms are responsible for perturbations to the global cloud fraction and RSDS. Indeed, the global-scale response in the atmospheric circulation induced by massive desert solar farms has been reported in an earlier study¹¹.

In North Africa, reduced surface albedo and feedbacks trigger localized warming and convection. This leads to surface convergence, and subsequently a positive geopotential height and divergence at the upper troposphere over North Africa (Fig. 4). The westerly anomalies due to surface convergence flow (Supplementary Fig. 2a, b) result in warming in the east and thus weakened tropical Atlantic zonal SST gradient, depicting an Atlantic Niño-like anomaly, particularly during the Western African Monsoon season²⁰ (Supplementary Fig. 2c, d). The Walker Circulation over the Pacific Ocean is intensified and expands westward due to these changes in the equatorial Atlantic

SST^{14,21} (Supplementary Fig. 5). It further leads to low-level southeasterly anomalies over the northern Indo-Pacific Ocean (Supplementary Fig. 2a, b), and hence an enhanced South Asian monsoon²². In turn, another anomalous anticyclone centered at west-central Asia is excited in the upper troposphere in NH summer (Fig. 4a, b) in response to enhanced South Asian monsoon. We analyzed the estimated vertical moist stability (VMS; Methods) over North Africa and India where stronger convection occurred (Fig. 5). The lower VMS driven by moisture convergence is found to induce increased total cloud fraction mainly due to more high cloud (Figs. 5 and 6). Decreased VMS and increased cloud cover in the surrounding regions such as southern Europe, Sahel, and Middle East can also be attributed to these processes.

During NH summer, the two baroclinic structures in North Africa and west-central Asia generate a Rossby wave train that propagates downstream following a mid-latitude westerly jet waveguide. Three barotropic structures (positive geopotential height) are generated over East Asia, the North Pacific and North America (Fig. 4a, b). Together, these upper tropospheric anomaly patterns resemble the wavenumber-5 circumglobal teleconnection pattern²³. The increased atmospheric thickness and anomalous anticyclone in the downstream regions provide unfavorable conditions for cloud formation in Japan and Eastern China, North Pacific, and Eastern US, mainly resulting in a decrease in mid and low cloud (Fig. 6). Specifically, mid and low cloud reductions over Eastern US mainly result from a divergent moisture flux and decreased dry static stability (Supplementary Fig. 6)²⁴. The cloud

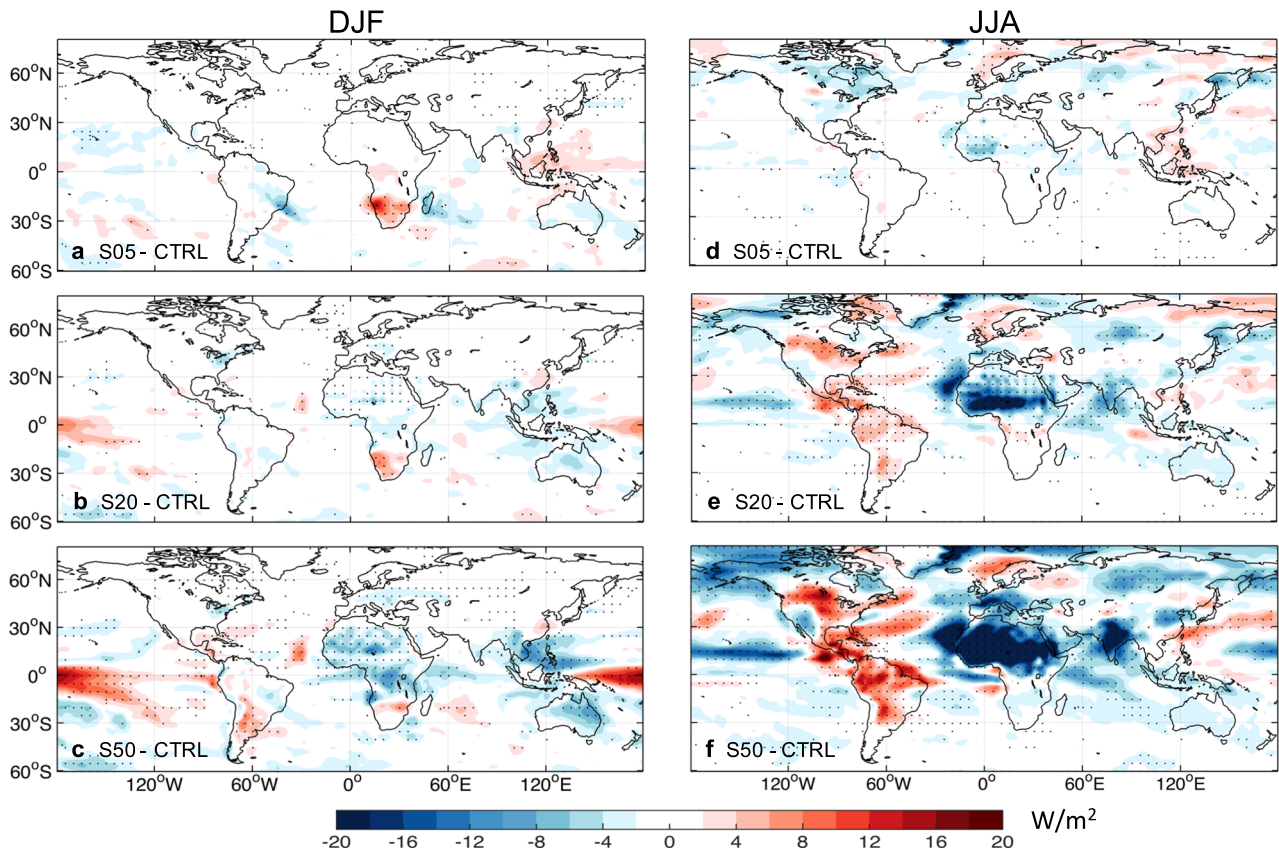


Fig. 2 Seasonal shortwave radiation affected by Sahara solar farms. **a-c** December-January-February (DJF) mean, **d-f** June-July-August (JJA) mean of RSDS response. Black dots depict anomalies that exceed 95% significance of *t* test.

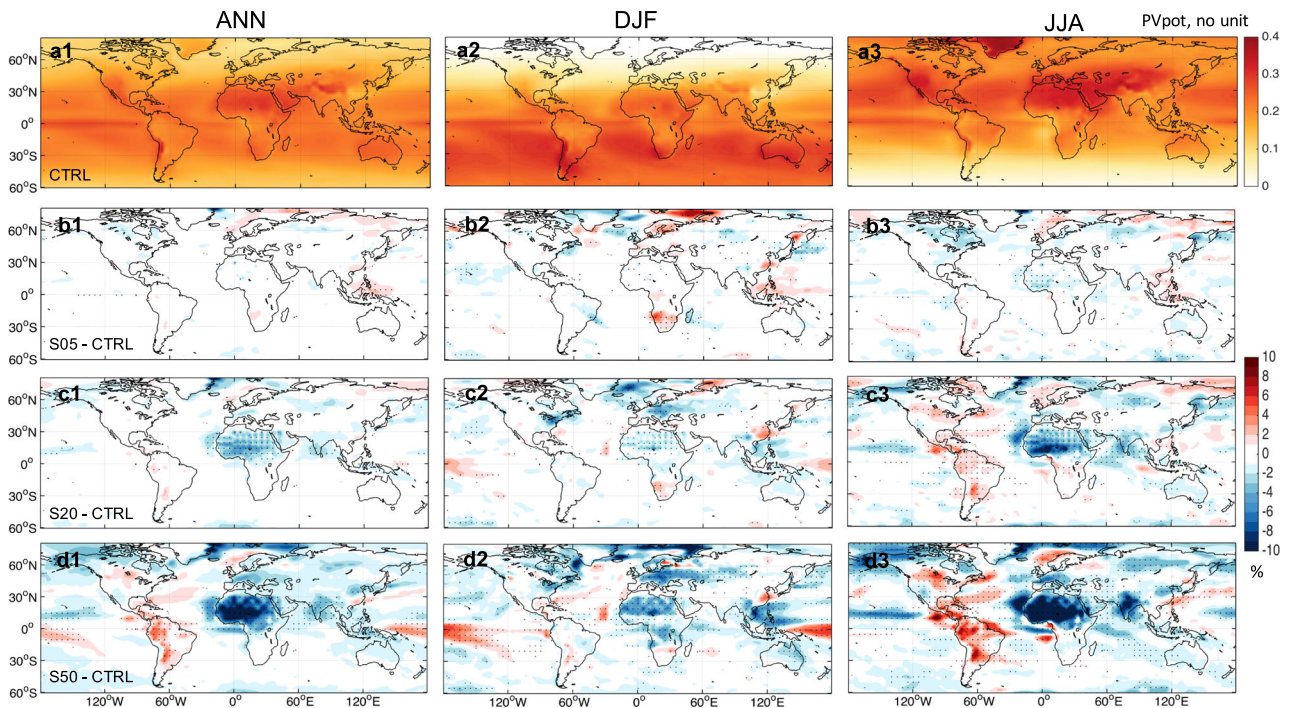


Fig. 3 Global solar potential affected by Sahara solar farms. **a1-a3** Map of ANN, DJF, JJA global PVpot in CTRL. **b-d** The annual mean, JJA mean and DJF mean changes in PVpot in S05, S20 and S50 simulations compared to CTRL. Black dots depict anomalies that exceed 95% significance of *t* test.

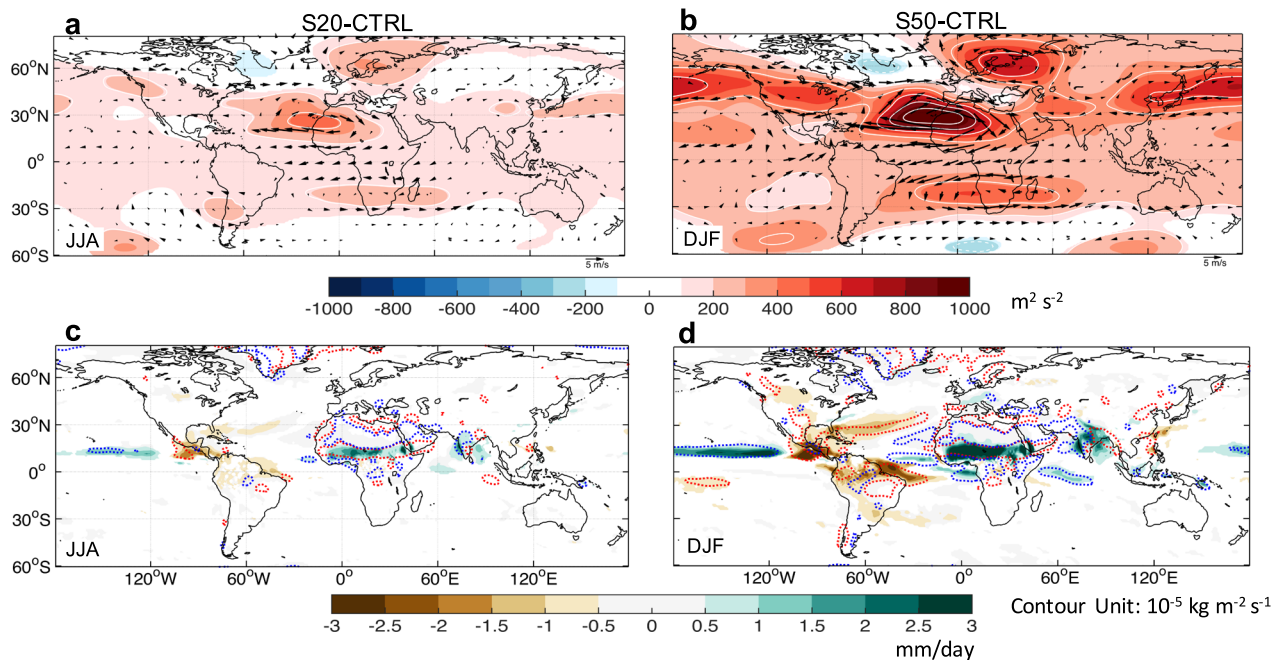


Fig. 4 Upper and lower troposphere response to Sahara solar farms. **a, b** JJA geopotential height and wind changes at 200 hPa; **c, d** JJA precipitation (shading) and divergence (contour, red = divergence, blue = convergence) at 850 hPa.

cover changes over Japan and North Pacific are not only associated with the anomalous anticyclonic circulation in the lower troposphere, but also influenced by a strengthened SST front of Kuroshio/Oyashio extension (Supplementary Fig. 2a, b) which also contributes to decreased dry static stability and low cloud over the southern flank of the SST front^{25,26}.

The strong heat source in North Africa triggers a Gill-type pattern^{27,28}. The pattern is characterized by local ascending motion in North Africa and a pair of descending motions to the west, over the extratropical North Atlantic and the Amazon (Fig. 4c, d). The southern center induces reduced high clouds in Brazil by reduced VMS. In addition, the moisture transport from both the tropical Atlantic and ITCZ in the Eastern Pacific is weakened, leading to reduced vertically integrated specific humidity (Fig. 5a, b) which also contribute to less cloud. The positive geopotential height and low-level divergence in North Europe is also linked to the Rossby wave response to the atmospheric heating in North Africa²⁹. Acting partly as a waveguide, the westerly jet stream over the North Atlantic induces a northeastward propagation of the Rossby wave from the cyclonic anomaly over the North Atlantic to North Europe. This Gill-type cyclonic anomaly links the atmospheric disturbance of the solar farms and the anticyclonic anomaly over North Europe, which further causes less cloud cover and more PVpot in that region.

The cloud cover change in the Southwestern US is opposite to that seen in the Central & Eastern US. More high clouds are seen in the southwestern states of the US (including Hawaii) (Fig. 6) where solar energy projects are currently expanding rapidly. This change is linked to the atmospheric river³⁰ that transports the rising moist air in the tropic Pacific to this region (Fig. 5a, b). In addition, a tight coupling between the mesoscale ocean processes (e.g. SST fronts, oceanic eddies) and the atmosphere over the Kuroshio and Oyashio regions (Supplementary Fig. 2c, d) helps to increase atmospheric river landfall in the Southwestern US^{31–33}.

The cloud changes discussed so far are stronger in NH summer than winter, even for South America. This highlights the direct

forcing from the Sahara region where the local response and land (vegetation)-atmosphere feedbacks are strongest during NH summer^{13,14}. Despite that, in Eastern Australia the largest anomalies occur in NH winter (Fig. 3). This seasonal difference indicates that local cloud conditions are more determined indirectly by remote forcing from North Africa, with a La Niña-like anomaly and strengthened and westward-extended Walker circulation (Supplementary Figs. 2 and 4) bringing wetter and cloudier conditions to Eastern Australia during local summer and wet season (Fig. 5a).

Discussion and conclusions

Our Earth system model simulations show that the envisioned large-scale solar farms in the Sahara Desert, if covering 20% or more of the area, can significantly influence atmospheric circulation and further induce cloud fraction and RSDS changes (summarized in Fig. 7) across other regions and seasons. Although the impacts are modest on a global or continental scale, the potential inequalities resulting from the disturbance of hypothetical Sahara solar farms can still manifest in the unequal distribution of solar power generation in many other regions where an energy transition to solar power is being heavily promoted, such as the Middle East, Europe, India, Eastern China, Japan, Eastern Australia, and Southwestern US. On the other hand, regions like Central and South America, the Caribbean, Central Eastern US, Scandinavia and South Africa may benefit from higher solar potential.

The research is a pilot case study in investigating how Saharan solar farms impact global solar power generation using one Earth system model and a limited number of scenarios. A caveat of this study is the use of a fixed *effective albedo* for PV solar panels, while in practical it varies with their type, efficiency, and operational condition (Supplementary Fig. 7)^{34,35}. Further, our solar farm simulations do not fully account for additional dynamical processes associated with other parameters of solar panels. For instance, previous studies have shown that surface roughness can

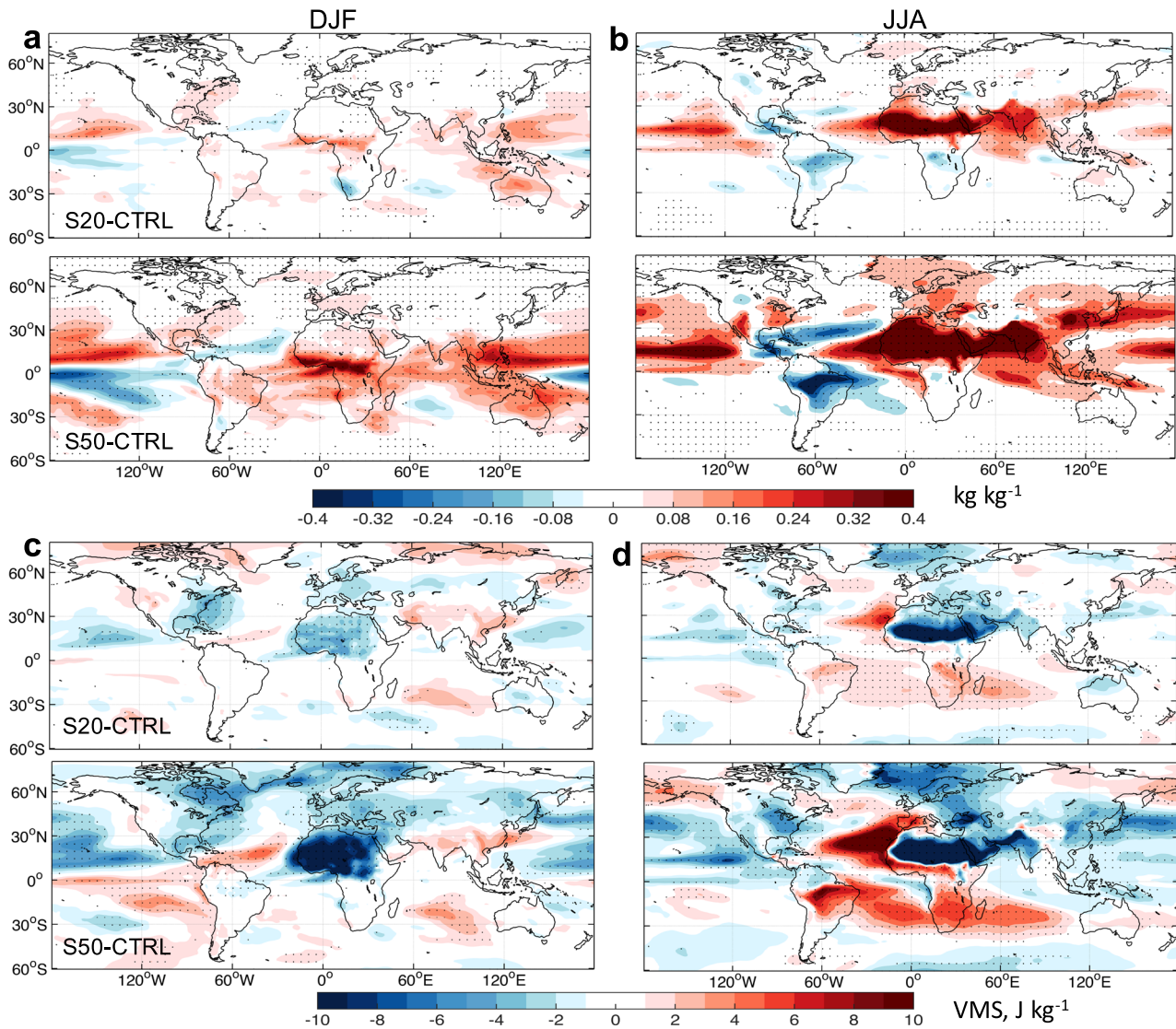


Fig. 5 Atmospheric stability response to Sahara solar farms. **a, b** vertically integrated specific humidity; **c, d** VMS changes. Lower VMS indicates a more unstable atmosphere.

potentially increase the efficiency of sensible heat transfer from the surface to the atmosphere in utility-scale solar farms¹².

More in-depth analyses and sensitivity simulations considering various scenarios combined with multiple Earth system models which overcome these limitations can shed more light on the impacts of this particular anthropogenic land use and land cover change. Future plans for the establishment of large-scale solar projects in global drylands by relevant stakeholders should be informed by these updated modeling studies to assess their potential impacts on the solar potential both locally and remotely (e.g. Supplementary Fig. 8). Improved understanding, thorough risk assessments and globally coordinated efforts are crucial in the world's solar energy transition to ensure enhanced energy security and equality.

Methods

The Earth system model EC-Earth. EC-Earth version 3.3.1 is a European community Earth system model (ESM)³⁶. It incorporates and couples model components treating atmosphere (ECMWF's IFS), ocean (NEMO), sea-ice (LIM) and land biosphere (LPJ-GUESS³⁷) processes, making it the EC-Earth-Veg-LR configuration capable of simulating complex interactions between

these model components, reflecting earth system feedbacks. The model's key performance metrics demonstrate physical behavior and biases well within the range of recent CMIP models^{36,38–40}. For specific comparisons, the readers should refer to “EC-Earth3-Veg” rather than “EC-Earth3” in these literature. EC-Earth reasonably reproduces several key dynamic processes relevant to this study, such as the atmospheric general circulation and monsoon system^{41,42}, atmospheric teleconnections^{20,43–45}, and clouds in the tropics⁴⁶ and the mid-latitudes over land (Supplementary Fig. 9).

The horizontal resolution of the atmosphere/land/vegetation gridcells is T159 (~1°), with 62 vertical levels in the atmosphere, while the ocean/sea-ice model has a horizontal resolution of ~1° and 75 vertical levels.

Solar farm simulations. We consider three Sahara solar farm scenarios, identified here as S05, S20 and S50, in which 5%, 20% and 50% of the model land gridcells in North Africa (15–30°N, 20°W–45°E) are prescribed as large photovoltaic (PV) solar panels. They are depicted by black dots in North Africa in Supplementary Fig. 1. Over the prescribed PV solar panels, the bare soil albedo was set to an *effective albedo* of 0.235^{13,14}.

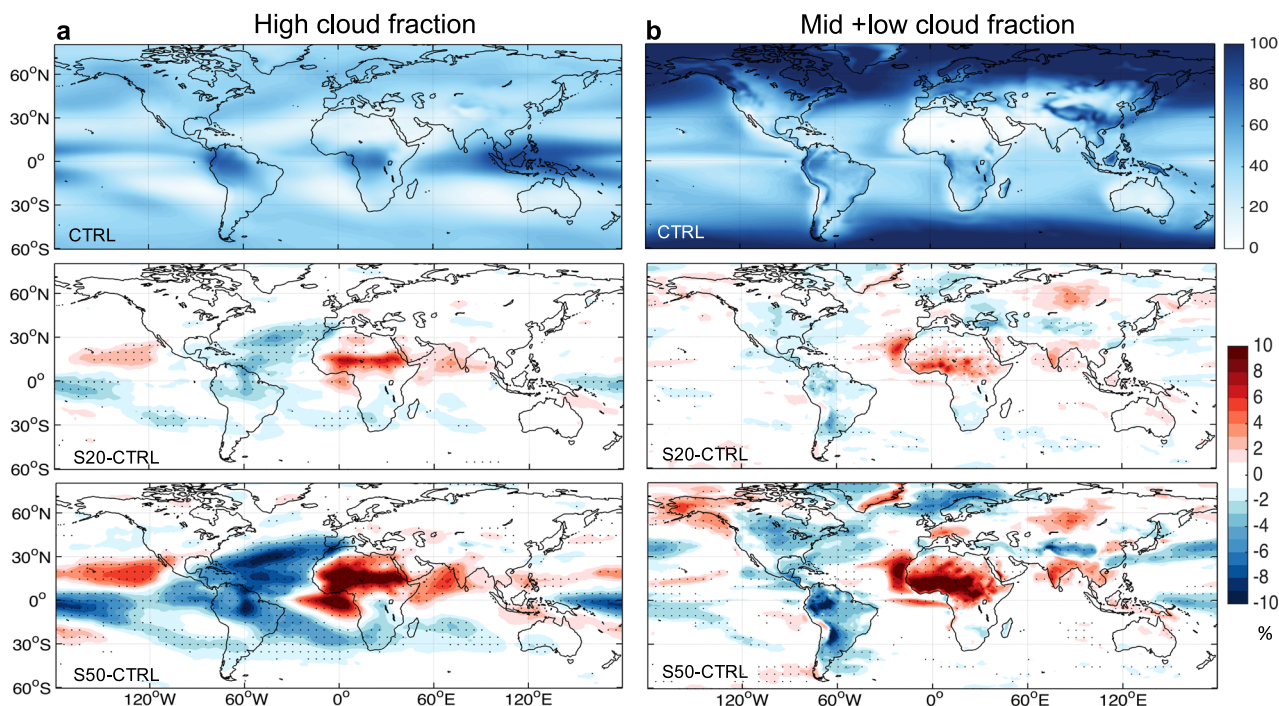


Fig. 6 Global cloud cover response at different levels. Modeled annual mean (a) High, (b) mid- and low cloud fraction changes. The upper panel shows values in the CTRL simulation, and the middle and lower panels show the response seen in the S20 and S50 experiments.

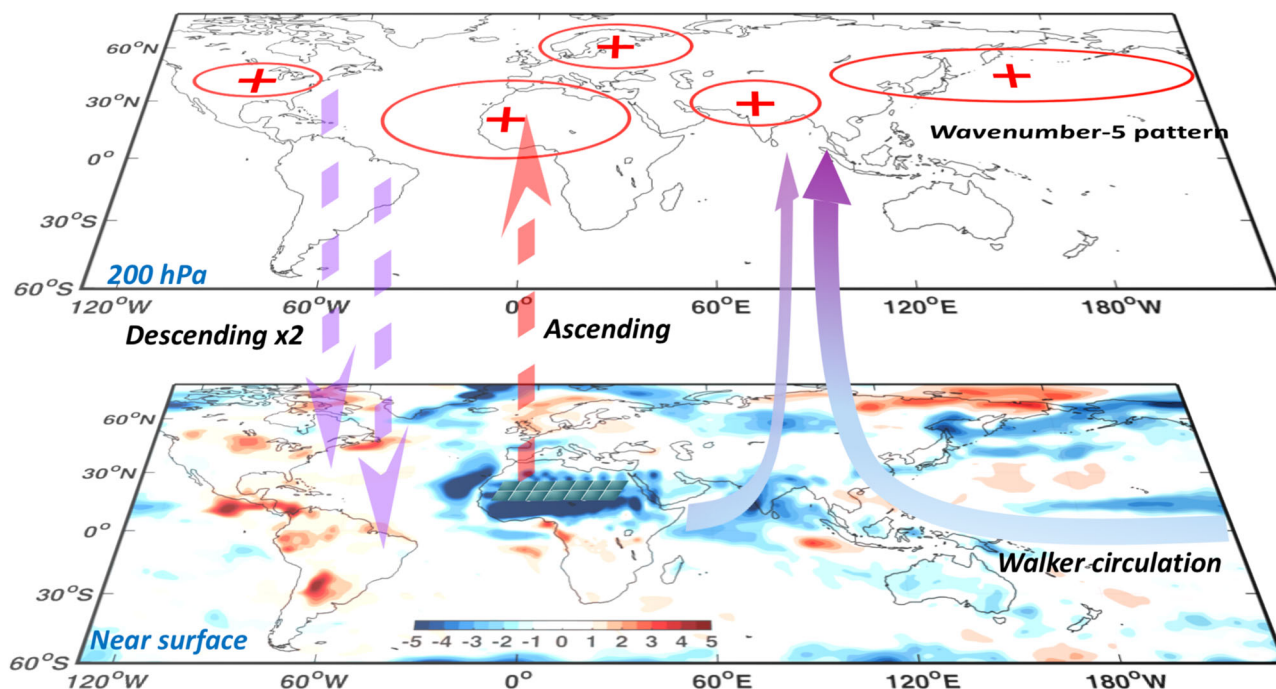


Fig. 7 The forcing mechanisms of Sahara solar farms on the atmospheric general circulation. A schematic plot summarizing the proposed mechanisms by which the global solar power generation is disturbed by large-scale Sahara photovoltaic solar farms. At the near surface layer, PVpot annual mean changes of S20-CTRL are shown (shading color). Positive centers in the upper atmosphere (200 hPa) show the wavenumber-5 structure of the circumglobal teleconnection over the Northern Hemisphere mid-latitudes, and another in Northern Europe representing a stationary Rossby wave relevant to a Gill-type pattern, all triggered by Sahara solar farms (illustrated in North Africa). Dashed arrows represent the ascent and descent of the atmospheric motion in a Gill-type pattern. The solid arrows over the surface in the tropics show the strengthened and westward-extended Walker circulation.

More justification of the 20% and 50% coverage we used can be found in Text S2 of refs. 13,14. These scenarios can be viewed from an energy production perspective, as follows.

S05: this scenario represents a potential energy option for the future world, considering the electricity it produces (~23.8 TW,

averaged over a year) roughly equals the world’s energy demand. The current global demand is ~18 TW^{13,14}.

S20: with tis electricity production is ~86.3 TW, this scenario, although ambitious, is not too far from real-world applications, considering factors like increased future energy consumption,

peak electricity demands, and substantial losses during power generation (conversion efficiency decreasing over time), storage and transport. S20 remains a tangible forecast.

S50: producing immense ~188.9 TW electricity, this scenario should be regarded as only an academic exercise, aiming for exploring the boundaries of global responses and better understanding of forcing mechanisms. It should be noted that the simulated responses can be underestimated due to the lack of potentially vital processes (e.g. the dust processes) in our simulations. Hence, S50 may provide an upper limit of the magnitude of responses for benchmarking.

We therefore focus on S05 and S20 results for quantification of solar farms impacts on the global solar power generation, and focus on S20 and S50 for diagnostics of the forcing mechanisms.

The *effective albedo* is the fraction of RSDS that does not heat the land surface, but instead is either directly reflected back to the atmosphere, or absorbed but converted to electricity. The electricity is considered exported so it does not generate heat locally. We assume a typical reflectivity of PV panels as 0.1⁴⁷ and a laboratory conversion efficiency of 0.15⁴⁸ for current commercial PV panels, and the *effective albedo* equals $0.1 + 0.15 \cdot (1 - 0.1) = 0.235$. This accounts for both the shortwave radiation reflected by the panels (0.1) and the solar energy converted to electricity (0.135) which does not generate heat locally. The concept of *effective albedo* has been widely used in earlier model simulations to investigate the climate impacts of solar panels^{11,13}. However, this study can be limited by the fact that it might underestimate the surface heating effect of PV solar panels on air when they generate electric power, particularly during daytime and summer.

The ESM simulations were initialized from a 1990CE climate (a default present-day climate state of EC-Earth) and integrated for 210 years to achieve a quasi-equilibrium state. To focus on the forcing effects of solar panels, the greenhouse gas levels, aerosol forcing and other land-use and land-cover properties were fixed at their 1990CE values. These boundary condition changes can also lead to climate change and thus impacts on solar power generation which has already been investigated in previous studies^{17–19}. The last 60 years of model output were processed and analyzed. To examine the impacts of initial and boundary conditions, we also conduct CTRL and S50 based on a climate state of 2010CE with fixed 2010CE greenhouse gases, land use, etc. The differences between the global surface air temperature and precipitation impacts under these two conditions (1990CE simulations vs. 2010CE simulations) yielded quite random patterns and marginal differences (Figure not shown). These results suggest that different initial and boundary conditions do not have significant impacts on our conclusions.

Similarly, we did four additional solar farms simulations in other drylands across the globe, namely, Central Asia, Central Australia and Southwestern US and Northwestern China, and examine their impacts on the global solar power generation. The global RSDS changes in these simulations are shown in Supplementary Fig. 8, and robust seasonal RSDS responses can be identified. The detailed investigation on the climate forcing mechanisms of solar farms in these region is beyond the scope of this study and will be pursued in upcoming research.

Estimates of PV power potential. The performance of PV cells depending on the weather conditions can be defined as the PV power generation potential (PVpot¹⁸). It is modulated in time by the energy resource RSDS(t), and PV cell temperature ($T_{cell}(t)$) that can affect the electrical efficiency⁴⁹.

$$PV_{pot}(t) = [1 + \gamma(T_{cell}(t) - T_{STC})] \frac{RSDS(t)}{RSDS_{STC}} \quad (1)$$

Where STC means the standard test conditions and $RSDS_{STC} = 1000 \text{ Wm}^{-2}$, $T_{STC} = 25 \text{ }^\circ\text{C}$ and γ equals $-0.005 \text{ }^\circ\text{C}^{-1}$. T_{cell} is taken as surface temperature simulated by EC-Earth. PVpot is 1 for STC, and it becomes lower (higher) than 1 when T_{cell} is higher (lower) than $25 \text{ }^\circ\text{C}$ and/or RSDS lower (higher) than 1000 Wm^{-2} .

Atmospheric stability analysis. The atmospheric stability can be quantified by the vertical moist stability (VMS⁵⁰), which is most effective when used as an indicator of the atmospheric convective stability over tropics at regional scales. It can be expressed as

$$VMS = MSE_{upper(200-500hPa)} - MSE_{lower(1000-700hPa)} \quad (2)$$

and can be understood as the difference between vertically integrated upper and lower layers of total moist static energy (MSE; unit: J/kg). We also used the lower-troposphere atmospheric dry static stability which is defined as the potential temperature difference between upper (700 hPa) and lower (925 hPa) level of the troposphere (modified from refs. 22,24). Note that both the indices apply better for the tropical and subtropical regions⁵⁰.

Data availability

The data related to the main figures in this study can be downloaded from <https://doi.org/10.5281/zenodo.10066990>.

Code availability

The Matlab codes for generating the main figures are available upon request to corresponding authors.

Received: 4 April 2023; Accepted: 15 November 2023;

Published online: 08 January 2024

References

1. IEA. *World Energy Outlook 2021*. (IEA, Paris, 2021).
2. IPCC. Global Warming of 1.5 °C: An IPCC Special Report on the impacts of global warming of 1.5 °C above pre-industrial levels and related global greenhouse gas emission pathways, in the context of strengthening the global response to the threat of climate change, sustainable development, and efforts to eradicate poverty. (Cambridge University Press, 2018) <https://doi.org/10.1017/9781009157940>.
3. Bogdanov, D. et al. Low-cost renewable electricity as the key driver of the global energy transition towards sustainability. *Energy* **227**, 120467 (2021).
4. Kannan, N. & Vakeesan, D. Solar energy for future world:-a review. *Renew. Sustain. Energy Rev.* **62**, 1092–1105 (2016).
5. Ehnberg, J. S. G. & Bollen, M. H. J. Simulation of global solar radiation based on cloud observations. *Solar Energy* **78**, 157–162 (2005).
6. Chen, C., Duan, S., Cai, T. & Liu, B. Online 24-h solar power forecasting based on weather type classification using artificial neural network. *Solar Energy* **85**, 2856–2870 (2011).
7. Ahmed, R., Sreeram, V., Mishra, Y. & Arif, M. D. A review and evaluation of the state-of-the-art in PV solar power forecasting: Techniques and optimization. *Renew. Sustain. Energy Rev.* **124**, 109792 (2020).
8. Staffell, I. & Pfenninger, S. The increasing impact of weather on electricity supply and demand. *Energy* **145**, 65–78 (2018).
9. Solaun, K. & Cerdá, E. Climate change impacts on renewable energy generation. A review of quantitative projections. *Renew. Sustain. Energy Rev.* **116**, 109415 (2019).
10. Cronin, J., Anandarajah, G. & Dessens, O. Climate change impacts on the energy system: a review of trends and gaps. *Clim. Change* **151**, 79–93 (2018).
11. Hu, A. et al. Impact of solar panels on global climate. *Nat. Clim. Change* **6**, 290–294 (2016).
12. Jiang, J., Gao, X., Lv, Q., Li, Z. & Li, P. Observed impacts of utility-scale photovoltaic plant on local air temperature and energy partitioning in the barren areas. *Renew. Energy* **174**, 157–169 (2021).
13. Li, Y. et al. Climate model shows large-scale wind and solar farms in the Sahara increase rain and vegetation. *Science* **361**, 1019–1022 (2018).
14. Lu, Z. et al. Impacts of large-scale Sahara solar farms on global climate and vegetation cover. *Geophys. Res. Lett.* **48**, e2020GL090789 (2021).

15. Dong, B., Sutton, R. T. & Wilcox, L. J. Decadal trends in surface solar radiation and cloud cover over the North Atlantic sector during the last four decades: drivers and physical processes. *Clim. Dyn.* **60**, 2533–2546 (2023).
16. Kushnir, Y., Robinson, W. A., Chang, P. & Robertson, A. W. The physical basis for predicting Atlantic sector seasonal-to-interannual climate variability. *J. Clim.* **19**, 5949–5970 (2006).
17. Hou, X., Wild, M., Folini, D., Kazadzis, S. & Wohland, J. Climate change impacts on solar power generation and its spatial variability in Europe based on CMIP6. *Earth Syst. Dyn.* **12**, 1099–1113 (2021).
18. Jerez, S. et al. The impact of climate change on photovoltaic power generation in Europe. *Nat. Commun.* **6**, 1–8 (2015).
19. He, Y. et al. Constrained future brightening of solar radiation and its implication for China's solar power. *Natl Sci. Rev.* **10**, nwa242 (2023).
20. Pausata, F. S. et al. Greening of the Sahara suppressed ENSO activity during the mid-Holocene. *Nat. Commun.* **8**, 16020 (2017).
21. Li, X., Xie, S.-P., Gille, S. T. & Yoo, C. Atlantic-induced pan-tropical climate change over the past three decades. *Nat. Clim. Change* **6**, 275–279 (2016).
22. Ning, L., Liu, J. & Sun, W. Influences of volcano eruptions on Asian Summer Monsoon over the last 110 years. *Sci. Rep.* **7**, 1–6 (2017).
23. Ding, Q. & Wang, B. Circumglobal teleconnection in the Northern Hemisphere summer. *J. Clim.* **18**, 3483–3505 (2005).
24. Klein, S. A. & Hartmann, D. L. The seasonal cycle of low stratiform clouds. *J. Clim.* **6**, 1587–1606 (1993).
25. Tokinaga, H. et al. Ocean frontal effects on the vertical development of clouds over the western North Pacific: In situ and satellite observations. *J. Clim.* **22**, 4241–4260 (2009).
26. Long, J., Zhang, S., Chen, Y., Liu, J. & Han, G. Impact of the Pacific–Japan teleconnection pattern on July sea fog over the northwestern Pacific: Interannual variations and global warming effect. *Adv. Atmos. Sci.* **33**, 511–521 (2016).
27. Gill, A. E. Some simple solutions for heat-induced tropical circulation. *Q. J. R. Meteorol. Soc.* **106**, 447–462 (1980).
28. Sun, W. et al. Northern Hemisphere land monsoon precipitation increased by the Green Sahara during middle Holocene. *Geophys. Res. Lett.* **46**, 9870–9879 (2019).
29. Yan, H. et al. Tropical African wildfire aerosols trigger teleconnections over mid-to-high latitudes of Northern Hemisphere in January. *Environ. Res. Lett.* **16**, 034025 (2021).
30. Gershunov, A. et al. Precipitation regime change in Western North America: the role of atmospheric rivers. *Sci. Rep.* **9**, 1–11 (2019).
31. Ma, X. et al. Distant influence of Kuroshio eddies on North Pacific weather patterns? *Sci. Rep.* **5**, 17785 (2015).
32. Long, J., Liu, C., Liu, Z. & Xu, J. Impact of the anomalous latent heat flux over the Kuroshio extension on Western North American rainfall in spring: Interannual variation and mechanism. *Front. Earth Sci.* **8**, 609619 (2021).
33. Wang, S. et al. Extreme atmospheric rivers in a warming climate. *Nat. Commun.* **14**, 3219 (2023).
34. Ying, J. et al. The characteristics and parameterizations of the surface albedo of a utility-scale photovoltaic plant in the Gobi Desert. *Theor. Appl. Climatol.* **151**, 1469–1481 (2023).
35. Li, Z. et al. A comparative study on surface energy flux characteristics of photovoltaic power station in Gobi in summer. *Theor. Appl. Climatol.* **148**, 1239–1247 (2022).
36. Döscher, R. et al. The EC-Earth3 Earth system model for the Coupled Model Intercomparison Project 6. *Geosci. Model Dev.* **15**, 2973–3020 (2022).
37. Smith, B. et al. Implications of incorporating N cycling and N limitations on primary production in an individual-based dynamic vegetation model. *Biogeosciences* **11**, 2027–2054 (2014).
38. Zhang, Q. et al. Simulating the mid-Holocene, last interglacial and mid-Pliocene climate with EC-Earth3-LR. *Geosci. Model Dev.* **14**, 1147–1169 (2021).
39. Parsons, L. A., Brennan, M. K., Wills, R. C. J. & Proistosescu, C. Magnitudes and spatial patterns of interdecadal temperature variability in CMIP6. *Geophys. Res. Lett.* **47**, e2019GL086588 (2020).
40. Di Virgilio, G. et al. Selecting CMIP6 GCMs for CORDEX dynamical downscaling: Model performance, independence, and climate change signals. *Earths Fut.* **10**, e2021EF002625 (2022).
41. Berntell, E., Zhang, Q., Chafik, L. & Körnich, H. Representation of multidecadal sahel rainfall variability in 20th Century reanalyses. *Sci. Rep.* **8**, 10937 (2018).
42. Pausata, F. S. R., Messori, G. & Zhang, Q. Impacts of dust reduction on the northward expansion of the African monsoon during the Green Sahara period. *Earth Planet. Sci. Lett.* **434**, 298–307 (2016).
43. Hazeleger, W. et al. EC-Earth: a seamless earth-system prediction approach in action. *Bull. Am. Meteorol. Soc.* **91**, 1357–1364 (2010).
44. Hazeleger, W. et al. EC-Earth V2. 2: description and validation of a new seamless earth system prediction model. *Clim. Dyn.* **39**, 2611–2629 (2012).
45. Kageyama, M. et al. The PMIP4 contribution to CMIP6–Part 4: Scientific objectives and experimental design of the PMIP4-CMIP6 Last Glacial Maximum experiments and PMIP4 sensitivity experiments. *Geosci. Model Dev.* **10**, 4035–4055 (2017).
46. Johansson, E. et al. Vertical structure of cloud radiative heating in the tropics: confronting the EC-Earth v3. 3.1/3P model with satellite observations. *Geosci. Model Dev.* **14**, 4087–4101 (2021).
47. Santbergen, R. & van Zolingen, R. J. C. The absorption factor of crystalline silicon PV cells: a numerical and experimental study. *Solar Energy Mater. Solar Cells* **92**, 432–444 (2008).
48. Green, M. A. et al. Solar cell efficiency tables (version 54). *Progr. Photovolt. Res. Appl.* **27**, 565–575 (2019).
49. Tonui, J. K. & Tripanagnostopoulos, Y. Performance improvement of PV/T solar collectors with natural air flow operation. *Solar Energy* **82**, 1–12 (2008).
50. Sharmila, S. & Walsh, K. J. E. Recent poleward shift of tropical cyclone formation linked to Hadley cell expansion. *Nat. Clim. Change* **8**, 730–736 (2018).

Acknowledgements

We acknowledge three anonymous reviewers for their constructive comments that have helped to improve the quality of the manuscript. Z.L. received funding from FORMAS mobility (Grant no. 2020-02267) and the Crafoord Foundation (Grant no. 20220564). This study is a contribution to the strategic research area MERGE and the Swedish Research Council (VR) funded project “Simulating green Sahara with Earth System Model” (2017-04232). The EC-Earth (developed by the EC-Earth consortium) simulations were performed on resources provided by the National Academic Infrastructure for Super-computing in Sweden (NAISS, projects S-CMIP, 2023/5-241 & SWESTORE) at Linköping University. J.L. is supported by the National Natural Science Foundation of China (Grant no. 41905006), China Scholarship Council (Grant no. 202108440322), Guangdong Provincial Observation and Research Station for Tropical Ocean Environment in Western Coastal Waters (GSTOE) and The key construction discipline of high-level universities-Marine science (Grant no. 231420003, 080503032101). J.X. is supported by the National Natural Science Foundation of China (Grant no. 72293604, 42130605).

Author contributions

Z.L., J.L. and Q.Z. conceived the study. Z.L. performed the simulations with input from Q.Z. and P.A.M. J.L. and Z.L. analyzed the data. P.A.M., B.S. and Q.Z. contributed to the development of EC-Earth-Veg-LR. Z.L. and J.L. wrote the first draft of the manuscript with contributions from all authors. All authors reviewed the manuscript.

Funding

Open access funding provided by Lund University.

Competing interests

The authors declare no competing interests.

Additional information

Supplementary information The online version contains supplementary material available at <https://doi.org/10.1038/s43247-023-01117-5>.

Correspondence and requests for materials should be addressed to Jingchao Long or Zhengyao Lu.

Peer review information *Communications Earth & Environment* thanks Aixue Hu, Xiaqing Gao, and the other, anonymous, reviewer(s) for their contribution to the peer review of this work. Primary Handling Editors: Pallav Purohit, Heike Langenberg. Peer reviewer reports are available.

Reprints and permission information is available at <http://www.nature.com/reprints>

Publisher's note Springer Nature remains neutral with regard to jurisdictional claims in published maps and institutional affiliations.



Open Access This article is licensed under a Creative Commons Attribution 4.0 International License, which permits use, sharing, adaptation, distribution and reproduction in any medium or format, as long as you give appropriate credit to the original author(s) and the source, provide a link to the Creative Commons license, and indicate if changes were made. The images or other third party material in this article are included in the article's Creative Commons license, unless indicated otherwise in a credit line to the material. If material is not included in the article's Creative Commons license and your intended use is not permitted by statutory regulation or exceeds the permitted use, you will need to obtain permission directly from the copyright holder. To view a copy of this license, visit <http://creativecommons.org/licenses/by/4.0/>.

© The Author(s) 2024